Title

Simultaneous multimaterial operando tomography of electrochemical devices.

Journal

Science Advances, 9(45)

Authors

Shrestha, Pranay

LaManna, Jacob

Fahy, Kieran

et al.

Publication Date

2023-11-10

DOI

10.1126/sciadv.adg8634

Peer reviewed

ELECTROCHEMISTRY

Simultaneous multimaterial operando tomography of electrochemical devices

Pranay Shrestha[1], Jacob M. LaManna[2], Kieran F. Fahy[1], Pascal Kim[1], ChungHyuk Lee[1,3], Jason K. Lee[1], Elias Baltic[2], David L. Jacobson[2], Daniel S. Hussey[2], Aimy Bazylak[1]*

The performance of electrochemical energy devices, such as fuel cells and batteries, is dictated by intricate physiochemical processes within. To better understand and rationally engineer these processes, we need robust operando characterization tools that detect and distinguish multiple interacting components/interfaces in high contrast. Here, we uniquely combine dual-modality tomography (simultaneous neutron and x-ray tomography) and advanced image processing (iterative reconstruction and metal artifact reduction) for high-contrast multimaterial imaging, with signal and contrast enhancements of up to 10 and 48 times, respectively, compared to conventional single-modality imaging. Targeted development and application of these methods to electrochemical devices allow us to resolve operando distributions of six interacting fuel cell components (including void space) with the highest reported pairwise contrast for simultaneous yet decoupled spatiotemporal characterization of component morphology and hydration. Such high-contrast tomography ushers in key gold standards for operando electrochemical characterization, with broader applicability to numerous multimaterial systems.

INTRODUCTION

Tomography (*1*) is a powerful nondestructive technique to evaluate material properties and distributions with applications in porous media (*2*), energy (*3*–*5*), earth science (*6*), life science (*7*, *8*), material science (*9*, *10*), archeology (*11*, *12*), and other diverse fields (*13*). In the context of electrochemical energy devices, such as fuel cells, batteries, and electrolyzers, advancements in tomography, especially using x-rays (*14*–*16*) or neutrons (*17*), have enabled detailed four-dimensional (4D; with three spatial dimensions and time) characterization of various cell components during electrochemical operation. Such operando imaging serves as a foundational platform to characterize and optimize mechanical, morphological, and transport properties of various materials, including membranes, porous layers such as gas diffusion layer (GDL), and flow fields (*18*, *19*).

Neutron and x-ray imaging each have unique advantages and limitations for operando imaging, and most studies so far focus on the use of one imaging modality at a time. X-rays interact with electrons, and the sensitivity or attenuation of x-rays generally increases with atomic number. In contrast, neutrons interact with atomic nuclei with no direct relationship between the atomic number and material attenuation, and materials such as hydrogen and lithium have a high opacity with neutrons [detailed comparison of attenuation cross sections for first 100 elements in the periodic table for neutrons at 2200 m s^{-1} and x-rays at 70 keV is shown in Fig. 1B; readers are also referred to the work by Kaestner *et al.* (*20*)]. For each modality, the attenuation cross section and opacity are dependent upon the energy level of x-rays or neutrons used for imaging and are primarily determined by the combination of the beam source and filters/moderators used (relationship between x-ray energy level and cross section highlighted in fig. S1). For neutron imaging, moderators are typically used to reduce the energy level of neutrons from the mega–electron volt range to the milli–electron volt range or lower ("thermal" neutrons and "cold" neutrons have energies greater than and less than 5 meV, respectively) (*21*). The dependence of material attenuation coefficient on energy level can be leveraged in methods such as wavelength-selective neutron imaging (*22*) to facilitate better detectability of materials.

In the context of operando polymer electrolyte membrane (PEM) fuel cell imaging, neutrons are particularly suited for high-contrast water detection due to high opacity of hydrogen with neutrons. Accurately characterizing liquid water distribution is crucial for PEM fuel cell development because liquid water management plays a key role in governing cell efficiency and durability, especially for high-performance fuel cells (*23*, *24*). Metal and metal-containing interfaces exhibit high opacity with x-rays, and x-ray imaging is well suited to track morphological evolution of interfaces such as the catalyst layer (CL)–PEM interface. X-ray imaging also typically benefits from higher spatial and temporal resolutions, whereby subsecond and submicron tomography have been recently developed and leveraged to study dynamic conditions. For instance, liquid water distribution may be resolved in working fuel cells to pinpoint pathways and mechanisms for water transport at varying commercially relevant operating conditions (*15*). X-ray tomography has also been used to track morphological characteristics of a full membrane electrode assembly (MEA) during degradation to reveal that degradation mechanisms in the membrane are strongly influenced by cell-scale heterogeneity of flow field lands and channels. Recently, advancements in the traditionally slower neutron tomography have made fast tomography (1.5-s scans) and dynamic imaging possible with cold neutron imaging (*17*, *25*), opening the possibility for high-contrast detection of water in dynamic and realistic conditions.

[1]Bazylak Group, Department of Mechanical & Industrial Engineering, Faculty of Applied Science and Engineering, University of Toronto, Toronto, Ontario, Canada. [2]Physical Measurement Laboratory, National Institute of Standards and Technology, Gaithersburg, MD, USA. [3]Department of Chemical Engineering, Toronto Metropolitan University, Toronto, Ontario, Canada.
*Corresponding author. Email: aimy.bazylak@utoronto.ca

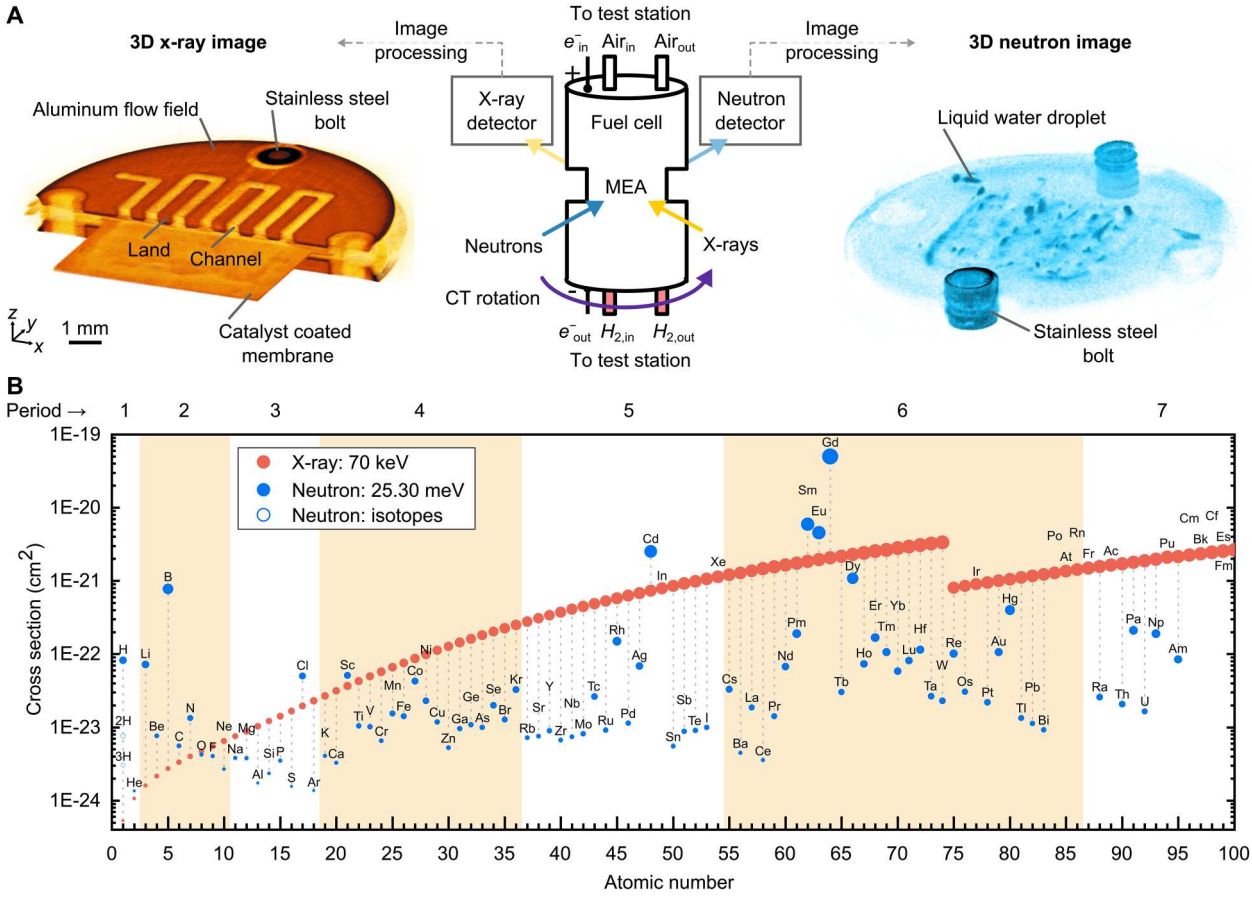

Fig. 1. Operando fuel cell setup for simultaneous neutron and x-ray tomography. (**A**) Fuel cell imaging schematic and sample neutron and x-ray images. Neutron and x-ray beams are oriented orthogonal to each other. The fuel cell is rotated 360°, and 701 equally spaced projections are collected. Image processing enhances the quality of 3D reconstructions of x-ray (thermal colormap) and neutron (blue) images, such that multiple interacting materials are visualized simultaneously in high contrast. Sample materials highlighted include liquid water droplets within channels visualized using neutron imaging and metal-containing components (CCM, aluminum flow fields, and stainless steel bolts) visualized using x-ray imaging. Axes for the 3D volumes are shown at the bottom left corner. Black scale bar (bottom left) for 3D reconstructions in (A) is 1 mm in length. CT, computed tomography. (**B**) Attenuation cross sections of the first 100 elements of the periodic table for thermal neutrons (25.30 meV) (*44*, *45*) and x-rays (70 keV) (*41*–*43*). Marker sizes scale with cross-sectional values in the log scale, and vertical shaded bands demark periods of the periodic table. Gray dotted lines indicate differences between neutron and x-ray cross sections for each element, highlighting opportunities for complementary imaging using dual-modality imaging at the given settings. Cross sections of hydrogen isotopes are shown to highlight that neutron imaging may be used to distinguish isotopes of elements. For a comprehensive map of x-ray cross sections for each element with varying x-ray energy levels, readers are referred to fig. S1.

However, further development is needed to enhance both temporal and spatial resolutions together for neutron imaging.

Combining x-ray and neutron images leverages the advantages of both techniques and reveals unique insights into the inner workings of electrochemical devices and other multimaterial systems. In some recent studies, authors correlate separately measured neutron and x-ray images of operando devices, such as batteries and fuel cells. For instance, Peng *et al.* (*5*) use operando neutron imaging and x-ray computed tomography to spatially and temporally locate liquid water distributions within alkaline membrane fuel cells. Operando insights enable them to recommend an improved electrode design that exhibits high performance and durability through efficient water management. In another study, Ziesche and co-workers (*3*) correlated nonsimultaneous 4D x-ray and neutron tomographs to identify mechanical degradation and lithium-ion transport mechanisms, respectively, in commercial lithium-batteries using a virtual unrolling technique. These studies show the promise of combining separately obtained neutron and x-ray images to reveal more insights than each single-modality image. However, electrochemical devices operate with complex and heterogenous physicochemical phenomena that are better suited for accurate characterization using simultaneous rather than separate applications of x-ray and neutron modalities.

Simultaneous neutron and x-ray tomography (NeXT) harnesses the true potential of both imaging modalities with stark compounding benefits, especially when used to track multiple interacting materials (*13*, *26*–*28*). Examples include in situ studies to characterize hydromechanical response of porous rocks (*29*) and ex situ characterization studies of battery electrodes (*30*), concrete (*31*, *32*), Martian rock samples (*13*), and archaeological artifacts (*12*). However, the application of simultaneous NeXT has not been extended to comprehensive and quantitative studies of operando processes in electrochemical devices. A practical bottleneck when considering operando imaging is the typical requirement of low

numbers of projections or low exposure times to facilitate fast scans, which leads to noisy reconstructed volumes using conventional image processing algorithms. Low noise and correspondingly high contrast and signal quality are desired in reconstructed images to detect and distinguish various materials of interest. For example, Xu *et al.* (*33*) demonstrate that the detection accuracy of liquid water is nearly 100% in x-ray images when the contrast-to-noise ratio (CNR) of water to void space is 6.6 (with no additional denoising) and that the detection accuracy is above 90% when the CNR is 2.2 (with mild denoising), respectively. Advanced image processing methods, such as iterative reconstruction (*34*–*36*) and artifact reduction techniques (*37*–*39*), offer a promising solution to overcome noise limitations in tomographic operando scans and facilitate quantitative analysis (*17*, *33*, *40*). However, there is a notable opportunity and need to combine the advancements in recent image processing tools with high-contrast imaging methods, such as NeXT to push the boundaries and capabilities of multimaterial operando imaging, especially in the context of electrochemical devices.

In this study, we present a unique combination of simultaneous dual-modality tomography (NeXT) and advanced image processing (iterative reconstruction and metal artifact reduction) for high-contrast multimaterial imaging and demonstrate signal and contrast enhancements of up to 10 and 48 times, respectively, compared to conventional single-modality imaging. We show that targeted development and application of such a high-contrast imaging method to electrochemical devices offer pronounced benefits, particularly the simultaneous and independent characterization of evolving MEA morphology and hydration. Accurate characterization of morphological and hydration characteristics in operando fuel cell materials is essential to advance modeling, optimization, and accurate prediction of performance and durability of next-generation fuel cells. From a method-development standpoint, this study highlights how advancements in hardware and software can be combined to yield marked enhancements in image quality/contrast and is generalizable to single- and multimodal imaging methods such as neutron, x-ray, and/or electron tomography. From an application standpoint, we highlight that directed innovation of imaging methods offers accurate and often exclusive characterizations of multimaterial systems. Although we emphasize the suitability of our methods to electrochemical devices, which span widespread and diverse technologies such as fuel cells, electrolyzers, batteries, and photoelectrochemical cells, the detailed methodology presented here is intended for seamless transfer and applicability to other operando and non-operando systems spanning topics such as physical/material science, life science, and geoscience.

RESULTS

Simultaneous dual-modality imaging

A custom fuel cell is operated and imaged using dual-modality simultaneous NeXT (Fig. 1A; details of the fuel cell and imaging setup are described in Materials and Methods). A key advantage of simultaneous dual-modality imaging is enhanced contrast between materials. The two imaging modalities have unique cross sections for each element of the periodic table at a given pair of energy levels [Fig. 1B; see also (*20*)] because x-rays (electromagnetic radiation) interact with electrons (*41*–*43*), while neutrons (*44*, *45*) (neutrally charged) interact with atomic nuclei. Differences in cross sections of neutron and x-ray imaging modes (dotted lines in Fig. 1B) offer opportunities for high-contrast complementary imaging. The range of imaging possibilities is further extended when considering isotopes for neutron imaging (highlighted for hydrogen isotopes for brevity in Fig. 1B) and energy levels (highlighted for x-rays imaging for brevity in Fig. S1). In this study, we leverage the complementarity of neutrons and x-rays for high-contrast tomography of electrochemical devices. In the context of fuel cells, neutrons are highly attenuated by hydrogen atoms; hence, neutron imaging is used to accurately locate and quantify *operando* liquid water distributions. X-rays are highly attenuated by metals; hence simultaneous x-ray imaging is used to track metal-containing components, such as aluminum flow fields (solid metal components that provide structural support and pathways for the transport of fluids through flow channels, and electrons and heat through the solid), and interfaces, such as the interface between a Pt-containing CL and the membrane. In addition, metals, such as Pt, are almost transparent to neutrons while water exhibits low opacity to x-rays. As a result, simultaneous NeXT allows us to decouple the characterization of liquid water and interfacial locations for high contrast independent characterization in the absence of material signal interference. This decoupling is of importance in *operando* imaging because unavoidable interfacial movement, such as membrane swelling, typically impedes the characterization of crucial interfacial properties in single-modality imaging. For instance, the complexity of resolving liquid water at the CL–GDL interface using single-modality x-ray imaging poses challenges when the *operando* movement of the membrane is involved (*40*, *46*).

Image processing enhances material contrast

Image processing is used to further enhance contrast between materials and enable detailed material characterizations (image processing routine detailed in Materials and Methods). In general, 2D projection images obtained using NeXT are processed, converted into sinograms, and then reconstructed into 3D volumes. In each of these stages, noise reduction techniques are used to enhance material detectability and contrast. The specific settings and details used for each image processing step are detailed in Materials and Methods and in Table 1. Here, we qualitatively and quantitatively present our findings of enhanced material contrast using two main image processing techniques: iterative reconstruction and metal artifact reduction.

An algebraic iterative reconstruction method, simultaneous iterative reconstruction technique (SIRT), is successful in suppressing noise to produce higher quality reconstructed volumes compared to noniterative filtered back projection (FBP) reconstruction. We choose this reconstruction technique, SIRT, because of its noise tolerance and robustness, especially when dealing with low numbers of projections and noisy projection images (for details of SIRT and FBP, see Materials and Methods). Our study provides a unique application of this well-established reconstruction technique to dual-modality images of operando fuel cells to highlight the potential of such methods to accurately characterize complex and heterogenous mechanisms within electrochemical devices. The enhancement in contrast and reconstruction quality is substantial when evaluating the CL region in x-ray images (Fig. 2). Signal and contrast are quantitatively assessed using signal-to-noise ratio (SNR) and CNR. High SNR and CNR are desirable for quantitative analysis; high SNR indicates high quality of signal compared to noise, while high CNR

Table 1. Image processing settings for neutron and x-ray images.

Image processing operation	Image processing settings		Software/ toolbox used
	Neutron images	X-ray images	
Image deconvolution	Point spread function: GadOx 85-mm PK 12; 3 pixels by 3 pixels median filter	N/A	NIST code (*26*)
Line noise filtering	Wavelet ring filter with filter size: 3 (small) and 83 (large); sigma: 1.5		NIST code (*26*)
Denoising (remove bright outliers)	Radius: 2 pixels; threshold: 25	N/A	Fiji (*58*)
Crop, tilt correction, and normalization	Subtract averaged dark-field image; correct for averaged flat-field image; rotate MEA plane to horizontal; crop region of interest (MEA and flow fields); normalize intensity with respect to open beam		NIST code (*26*)
Sinogram generation	Calculate axis of rotation using central cell feature; ring removal (Vo stripe filter) with signal to noise ratio: 3; stripe median filter: 3 (small) and 55 (large)		NIST code (*26*)
Metal artifact reduction	N/A	Metal bolts segmented in 3D volume to obtain metal trace that is subtracted from original sinogram; linear interpolation is used to fill subtracted sinogram regions	MAR-LI (MATLAB) (*37*)
General reconstruction settings	A total of 701 equally spaced projections in 360°; source-to-detector distance: 6000 mm; source-to-object distance: 5960 mm; rotation: clockwise; detector pixel size: 0.009 mm	A total of 701 equally spaced projections in 360°; source-to-detector distance: 610 mm; source-to-object distance: 305 mm; rotation: counterclockwise; detector pixel size: 0.0169 mm	Octopus (*60*)/ ASTRA toolbox (MATLAB) (*35*, *59*)
Noniterative reconstruction (FBP)	Filtered back projection with automated detection of center of rotation (fine adjustment) and beam center		Octopus (*60*)
Iterative reconstruction (SIRT)	ASTRA function used: "SIRT3D_CUDA" with 150 iterations	Self-calibrated cone-beam in sinograms (*65*); ASTRA function used: "SIRT3D_CUDA" with 150 iterations	ASTRA toolbox (MATLAB) (*35*, *61*)
Volume registration	Multimodal volume registration with affine transformation (scale, rotate, and translate) with maximum iterations of 10,000; downsized by 5^3 for to calculate transformations		NIST code (*26*)

between materials indicated high contrast and discernability between materials in 3D (details of SNR and CNR quantification are provided in Materials and Methods). Quantitatively, SNR and CNR values of the CL (calculated in gray dashed boxes shown in Fig. 2A) are enhanced by 3.3× (2.9 to 12.5) and 4.3× (3.0 to 15.8), respectively, when using SIRT instead of FBP. Higher SNR and CNR values due to iterative reconstruction are manifested as clearly defined and distinguishable features. Enhanced contrast of the CL enables us to precisely locate and characterize the 4D morphology of the catalyst-coated membrane (CCM) as well as the adjacent GDLs.

In essence, SIRT reconstructions facilitate our detection of subtle microstructural deformations of the membrane corresponding to land-channel patterns, whereby the CCM is seen to bend at the channel regions (shown using green arrows in Fig. 2F, but not visible in Fig. 2E). This membrane deformation manifests as alternating peaks of catalyst signal (gray values of 0.07) and valleys of background signal (gray values of 0.05) when analyzing the gray values of a straight-line segment (black dashed line in Fig. 2, B and D) across the CCM at the land-channel regions (Fig. 2F). Land-channel imprints are also observed in the cross-sectional slice (top) in SIRT reconstructions (Fig. 2B). In contrast, the magnitude of noise in gray values in FBP reconstructions is on the order of catalyst peaks and renders the CL almost indistinguishable from background (Fig. 2, A, C, and E). Furthermore, typical smoothing/filtering techniques, such as 3D median filtering, fail to preserve 3D morphological details of the CL, despite showing some enhancements in CNR and SNR values (details in fig. S2). Identifying the microscale heterogeneity in the CCM morphology is vital for accurately characterizing the mechanical and hydration properties of membranes, and these steps are necessary for realizing predictive models for fuel cell performance and durability (*23*, *24*, *46*).

In neutron images, water droplets in the flow field channels and the under-land regions of the GDL are clearly distinguishable (Fig. 3). Quantitatively, SNR and CNR improve by 0.6× (6.2 to 9.9) and 0.7× (7.8 to 13.5), respectively, when the reconstruction method is changed from noniterative FBP to iterative SIRT. The distinguishability of liquid water from the background is also evaluated using a gray value profile of a line segment (shown in black dashed line in Fig. 3). The gray value profile for SIRT exhibits a smoother profile (indicating less noise) and more distinguishable intensity regions for liquid water within the channels and in the GDL under the lands (shown in Fig. 3, B and D), when compared to conventional FBP. Enhancements in contrast/signal quality, corresponding to higher CNR/SNR values, signify a more pronounced distinction between a signal of interest and the background/noise, and these enhancements also enable more accurate distinguishability/detection for the quantitative analysis of materials.

Highly attenuating materials, such as metals (stainless steel bolts in this study), tend to produce streak artifacts in reconstructed x-ray images due to underlying effects, which include beam hardening, scattering, noise, and photon starvation (*47*). For this study, we use a simple artifact correction technique, called metal artifact reduction–linear interpolation (MAR-LI; details in Materials and Methods). MAR-LI is effective at removing streak artifacts due to the highly attenuating stainless steel bolts (Fig. 4). Before MAR-LI, streak artifacts are clearly visible in the cross-sectional x-ray image of the PEM region, whereby darker (higher gray value) and lighter (lower gray value) bands or "streaks" are observed stemming from the edges of the bolts (indicated with black arrows in Fig. 4A).

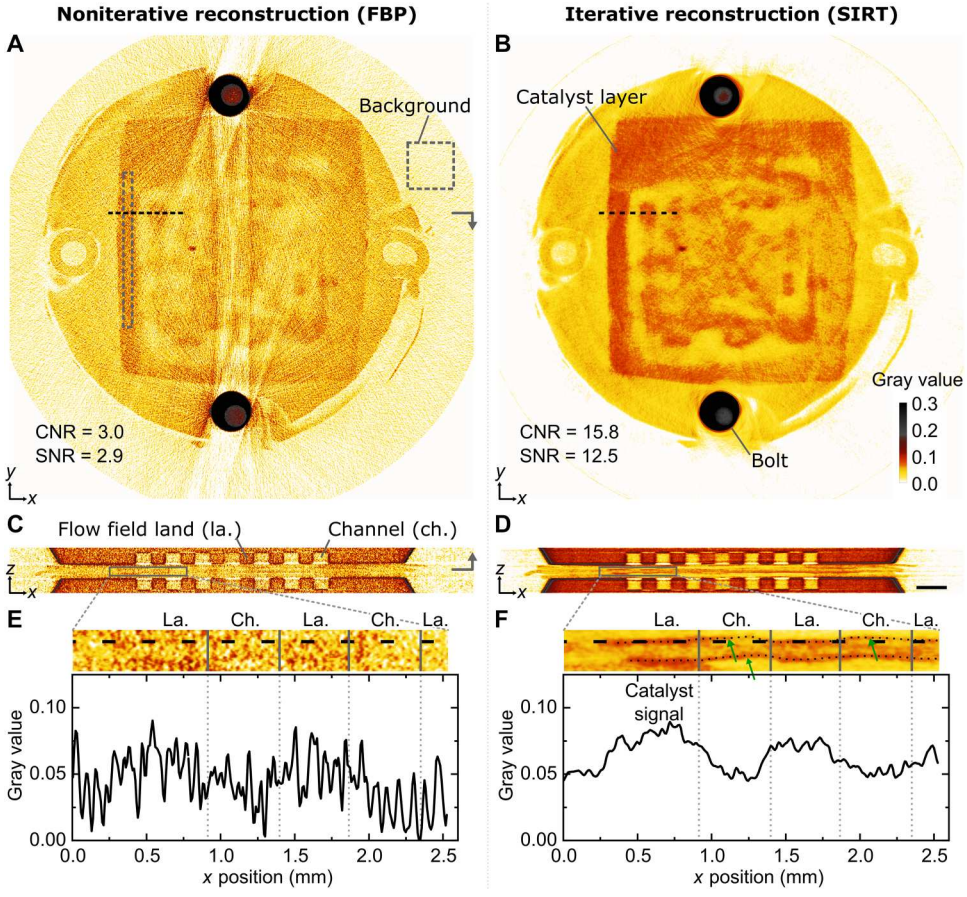

Fig. 2. Comparison of conventional noniterative reconstruction (FBP) and proposed iterative reconstruction (SIRT) methods for x-ray images. Cross-sectional slice of top (**A** and **B**) and side (**C** and **D**) views showing the catalyst layer (CL), which is coated on the membrane [gray arrow in (A) indicates the *y* location of slice C, while gray arrow in (C) indicates the *z* location of slice A]. Gray dashed boxes in (A) for the CL and background regions are used to calculate SNR and CNR. Iterative reconstruction enhanced SNR and CNR for the CL by 3.3× and 4.3×, respectively, when compared with conventional FBP reconstruction. Gray value profiles of sample line segment [black dashed line in (A), (B), (**E**), and (**F**)] for (E) FBP and (F) SIRT reconstructions. The gray value profiles quantitatively highlight enhanced contrast and distinguishability of the CL from the background due to iterative reconstruction. High SNR and CNR reveal subtle microstructural deformations of the membrane aligned with land and channels, visible in enlarged side profiles in (F) SIRT reconstructions (indicated with green arrows) but not in (E) FBP reconstructions. A low CL signal is observed under the channels in (F) due to membrane curvature (highlighted using green arrows), which leads to CL misalignment (with the black straight dashed line of reference). Color bar (bottom right) in (B) is scaled to effectively visualize the CL. Black scale bar (bottom right) in (D) is 1 mm in length [applicable for (A) to (D)]. Spatial axes are shown on bottom left in (A) to (D).

The streaks also show up as peaks and valleys distinct from the background PEM in the gray value profiles (Fig. 4C). In comparison, after MAR-LI, the PEM region, especially the central region of interest, seems unaffected by such streaks (Fig. 4B) with a relatively uniform gray value profile devoid of spikes (Fig. 4A). To assess the effectiveness of the MAR-LI algorithm, we focus our analysis on the bulk PEM region because we expect a homogenous intensity profile in the x-ray images at this region. The presence of a homogenous intensity profile in the 2D images and 1D line profiles indicates that the implemented algorithm has been effective. Quantitatively, we observe a reduction in streak artifacts by up to 94%, whereby the maximum amplitude of gray value of the streaks reduced from 0.035 to merely 0.002, before and after MAR-LI, respectively. Although more sophisticated streak removal algorithms are available and may be suitable for more complex images (*37*, *38*, *48*), a simpler method based on linear interpolation is adopted here because of its effectiveness on our dataset.

Techniques such as MAR-LI allow us to preserve the high contrast of strongly attenuating materials, such as metals, without suffering from the drawback of streak artifacts in 3D reconstruction, and effectively increase the range of detectable and quantifiable materials in 3D imaging. To avoid streak artifacts altogether, highly attenuating materials such as metal bolts may be removed from the design of the cell [as in some previous works (*14*, *15*)], which is a viable and convenient option for some systems like custom fuel cells. However, in some other systems such as batteries, metal is an integral component of the cell (*19*), in which case correction techniques like MAR-LI would be highly valuable for accurate quantification, especially during operando imaging. In this study, we highlight the benefits of processing tools such as MAR-LI to extend the applicability of proposed high-contrast imaging to a broader range of devices and systems.

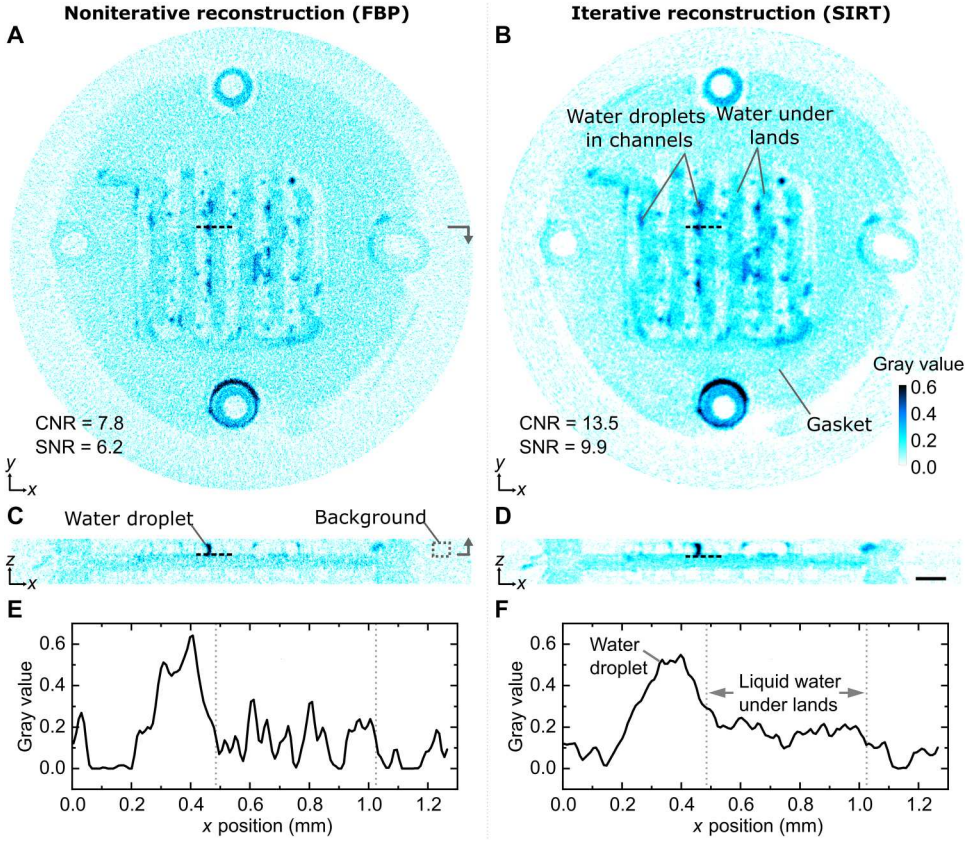

Fig. 3. Comparison of conventional noniterative reconstruction (FBP) and proposed iterative reconstruction (SIRT) methods for neutron images. Cross-sectional slice of top (**A** and **B**) and side (**C** and **D**) views showing water droplets within the flow field channels and water in the GDL under the lands [gray arrow in (A) indicates the *y* location of slice C, while gray arrow in (C) indicates the *z* location of slice A]. Gray value profiles of the line segment [black dashed line in (A) to (D)] for (**E**) FBP and (**F**) SIRT reconstructions, which quantitatively highlight enhanced contrast and distinguishability of liquid water from background. Land and channel regions are demarked using gray dashed lines in (E) and (F). Liquid water droplets within channels (average of five instances) and background [gray dashed box indicated in (C)] are used to calculate SNR and CNR. Iterative reconstruction enhanced SNR and CNR for the liquid water by 0.6× and 0.7×, respectively when compared with conventional FBP reconstruction. Color bar (bottom right) in (B) is scaled to highlight liquid water. Black scale bar (bottom right) in (D) is 1 mm in length [applicable for (A) to (D)]. Spatial axes are shown on bottom left in (A) to (D).

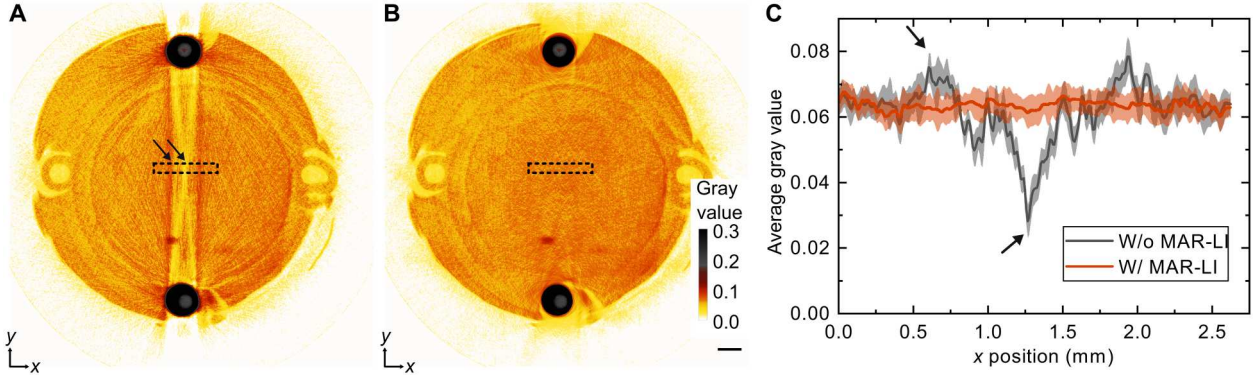

Fig. 4. Metal artifact reduction–linear interpolation. (**A**) Streak artifacts from stainless steel bolts in x-ray imaging (indicated using black arrows) in a cross-sectional image of the PEM region. (**B**) Metal artifacts corrected using linear interpolation of sinograms at regions affected by highly attenuating metal bolt, using a technique called MAR-LI (*37*). (**C**) Average gray value profile along the *x* direction in the boxed region indicated in (A) and (B). Average and SD of gray values at each *x* position are shown using solid lines and shaded regions, respectively. Black scale bar (bottom right) in (B) is 1 mm in length. Using MAR-LI, streaks (shown in black arrows) are successfully reduced by up to 94%. Spatial axes are shown on bottom left in (A) and (B).

Toward correlative and quantitative NeXT

The benefits of advanced image processing (here, iterative reconstruction and MAR-LI) are compounded when both neutron and x-ray modalities are combined and correlated (sample correlated 3D image shown in Fig. 5A and movie S1). Between x-ray and neutron images, the imaging modality with higher signal/contrast quality (higher SNR/CNR) for a given material/material pair is chosen as the dominant modality and used to detect/distinguish the material; e.g., neutron imaging is used to detect liquid water because SNR/CNR values (with respect to void) for water are 9.9/13.5 and 2.9/3.9 for neutron and x-ray imaging, respectively. Water distribution characterized using neutrons is accurately contextualized in 3D using locations of fuel cell components and interfaces characterized using x-rays (Fig. 5A and movie S1). For quantitative analysis, a pairwise contrast matrix is constructed to evaluate the contrast and distinguishability between six components of interest: CL, water droplets, aluminum flow field (Al), PEM, stainless steel bolt (SS bolt), and void space. Using dual-modality NeXT imaging and advanced image processing, six distinct components of interest (including void space) are distinguished with mean and median CNR of 9.5 (Fig. 5B; details on the calculation and interpretation of a correlative contrast matrix are provided in Materials and Methods). Correlative SNR for all materials except background void space was greater than 6.6 (table S1). Overall, with advanced image processing alone, correlative CNR and SNR are enhanced by up to 7.1× (fig. S3) and 5.9× (table S1), respectively. The proposed high-contrast imaging method (combination of NeXT and advanced processing) provides even greater benefits when compared to the less dominant mode of single-modality imaging with conventional image processing, whereby CNR and SNR values are 2 to 48 times and 2 to 10 times higher, respectively (Fig. 5B). Such marked improvements in CNR and SNR values push the frontier for simultaneous characterization of multiple materials with high accuracy and quantitative potential.

A key advantage of dual-modality simultaneous NeXT imaging is the capability of characterizing interacting materials simultaneously and independently, without interference of material signals. An effective method to decouple the characterization of interacting materials, such as liquid water and CL, is to exclusively use an imaging modality as the dominant mode to characterize a material. A prerequisite for such decoupling is high signal (SNR) and contrast (CNR) for materials in the dominant modality, but high transparency (low SNR and CNR with void) in the unused modality. In this study, liquid water is characterized using neutrons with high SNR of 9.9, while the CL is characterized using x-rays with an SNR of 12.5. Considering the unused imaging modality, liquid water has a low SNR/CNR with void of 2.9/3.9 in x-rays, while the CL has an SNR/CNR with void of 1.9/2.3 in neutrons, making the materials nearly transparent in the unused imaging modality. Although post-processing methods such as image subtraction may be used to effectively increase contrast and detection accuracy of low-opacity materials such as liquid water in x-ray images (*14*, *33*), high transparency of materials in the unused modality offers low signal interference with the other high-opacity materials in that modality, facilitating nearly independent characterization of certain materials. Independent characterization of liquid water and CL is important in accurately quantifying interfacial, morphological, and hydration properties in operating fuel cells (*5*, *46*). For this study, all the materials of interest (except void space) had high SNRs of greater than 6.6 in the dominant imaging modality and low SNRs of less than 2.9 (except SS bolt with SNR of 5.1) in the unused imaging modality.

Applicability to other electrochemical devices and multimaterial systems

We highlight and demonstrate broad relevance of our methods to other electrochemical devices and multimaterial systems by applying the combination of NeXT and advanced image processing to a pristine alkaline battery (LR41, PKCell; with neutron and x-ray voxel sizes of 8.96 and 8.48 μm, and all other beam, camera, and SIRT image processing settings identical to those used for operando imaging of fuel cells, as detailed in Methods and Materials). The combination of dual-modality NeXT and advanced image

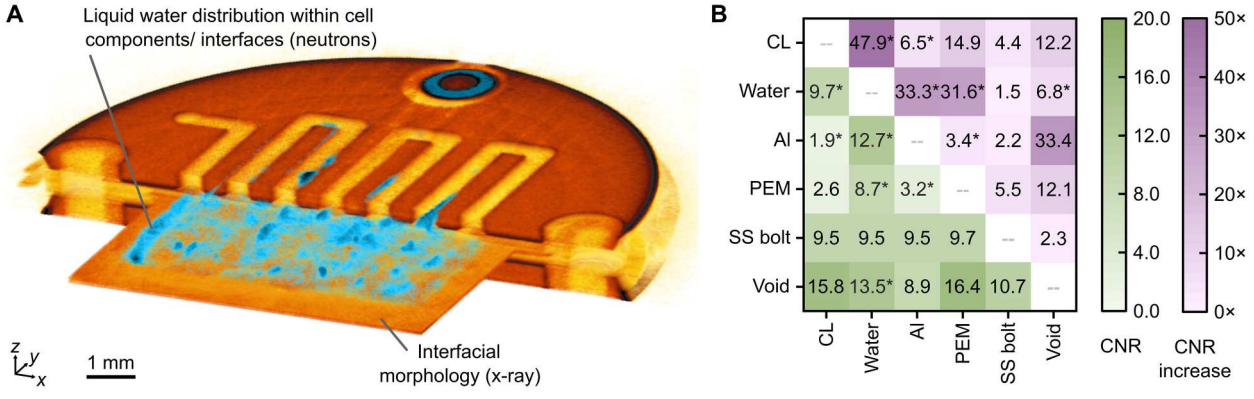

Fig. 5. Correlative dual-modality operando image and correlative contrast matrix. (**A**) Correlative 3D image of neutron and x-rays shown with cutouts for clarity. Dual-modality imaging and advanced image processing enables visualization of multiple interacting materials, such as liquid water and metal interfaces and components, with high contrast. Black scale bar in (A) is 1 mm in length. (**B**) Correlative contrast matrix of six components within the fuel cell: catalyst layer (CL), water droplets, aluminum flow field (Al), PEM, stainless steel bolt (SS bolt), and void space. CNR is shown in green color scale, and enhancement in CNR due to advanced image processing and dual-modality imaging is presented in purple color scale. Between neutrons and x-rays, the imaging modality with higher CNR is chosen to detect the material of interest and shown in the matrix (bottom triangle with green color scale). When neutron is the dominant modality used for material detection, values are shown with * in the matrix. The proposed high-contrast imaging method provides pronounced enhancements in material contrast compared to single-modality imaging with conventional image processing (shown in top triangle with purple color scale).

processing enables us to resolve six key battery components in high contrast: anode (Zn), electrolyte, separator, cathode (MnO_2), gasket, and casing (Fig. 6). The highly complementary nature of neutrons and x-rays in NeXT is advantageous for battery characterization (as in the case for fuel cell imaging). Metal components such as zinc anode, manganese dioxide cathode, and outer casing are resolved with high signal/contrast in x-rays, while neutrons enable high-quality detection of polymers and hydrogen-containing materials, such as gasket, alkaline electrolyte, and separator. As seen with fuel cell imaging, combining image processing advancements with NeXT yields compounding benefits for battery imaging, whereby signal (table S2) and contrast (Fig. 6B) are markedly enhanced compared to single-modality imaging with conventional FBP processing (CNR and SNR enhancements of up to 446× and 42×, respectively). Such enhancements in image contrast and quality allows us to accurately map the spatiotemporal distributions of battery components (including subtle features such as cracks in the cathode, gray arrow in Fig. 6A), which is essential for the development of next-generation batteries and electrochemical devices.

DISCUSSION

By targeted pairing of dual-modality imaging and advanced imaging processing, we visualize and resolve six interacting fuel cell components (including void space) simultaneously during operation in high contrast. CL and liquid water are distinguished independently and simultaneously using x-rays (SNR of 12.5) and neutrons (SNR of 9.9), respectively, with a pairwise CNR value of 9.7. We find that image processing is key to enhancing contrast, whereby CNR and SNR enhancements of up to 7.1 and 5.9 times are observed. More specifically, iterative reconstruction enhances CNR/SNR by 4.3×/3.3× and 0.7×/0.6× for characterization of CL via x-rays and liquid water droplets via neutrons, when compared with conventional noniterative reconstruction. MAR-LI successfully corrects for streak artifacts from highly attenuating stainless steel bolts while still preserving the bolt in the images (94% reduction in artifacts). A unique analysis of correlative signal and contrast matrix reveals tremendous benefits of applying dual-modality imaging with proposed image processing, with contrast and signal enhancements of up to 48 and 10 times, respectively, compared to single-modality imaging with conventional processing. Enhancements in material contrast reveal subtle microstructural deformation of the CCM and heterogeneity in liquid water accumulation with respect to land-channel patterns. Furthermore, decoupled characterization of liquid water and metal interfaces enables accurate contextualization of liquid water in evolving components and interfaces of the fuel cell. For instance, this decoupled characterization is particularly insightful when accessing the relationship between liquid water and the heterogenous evolution of membrane interfaces, which has implications for membrane durability and long-term fuel cell performance (*49*). By accurately characterizing the 4D distribution of liquid water and membrane interfaces independently, we can more accurately model the hygroscopic behavior of the membrane, which, in turn, can be used to optimize fuel cell performance and durability.

Regarding potential avenues for future work, NeXT is ripe for even further development and advancements. Leveraging innovations in cold neutron imaging (*17*), wavelength-selective (*22*) and high-resolution neutron imaging (*25*, *50*, *51*), high-quality desktop x-ray systems (*1*, *9*, *52*, *53*), and operando-specific image processing (*17*, *33*, *34*, *40*, *54*), high-contrast NeXT imaging is poised to realize even higher fidelity and more dynamic scans than those presented here. Furthermore, in this study, a separate analysis of x-ray and neutron histograms is sufficient to provide necessary contrast for material distinguishability. The two histograms may be combined into a bivariate histogram to further enhance distinguishability using bivariate phase segmentation (*26*, *28*, *31*). In addition, transient materials in operando processes may be quantified accurately using image subtraction. For instance, the appearance or accumulation of liquid water may be quantified by

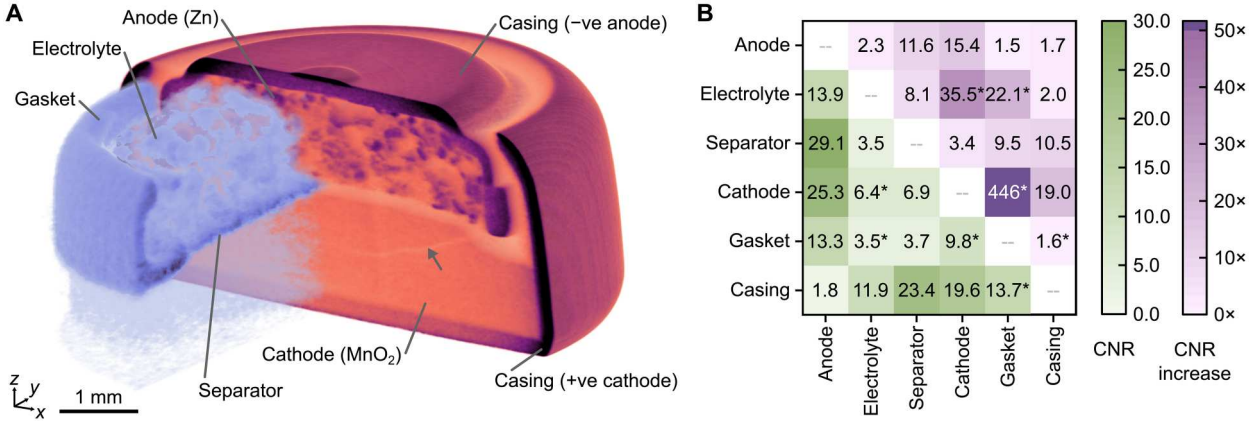

Fig. 6. Dual-modality image and contrast matrix for alkaline battery to demonstrate generalized applicability of methods. (**A**) 3D image of neutron and x-rays of a pristine alkaline battery shown with cutouts for clarity. Six key components within the battery are shown: anode (Zn), electrolyte, separator, cathode (MnO_2), gasket, and casing. Subtle features such as crack in the cathode (gray arrow) are observed. Black scale bar in (A) is 1 mm in length. (**B**) Correlative contrast matrix of key battery components. CNR is shown in green color scale, and enhancement in CNR due to advanced image processing and dual-modality imaging is presented in purple color scale. Between neutrons and x-rays, the imaging modality with higher CNR is chosen to detect the material of interest and shown in the matrix (bottom triangle with green color scale). When neutron is the dominant modality used for material detection, values are shown with * in the matrix. The proposed high-contrast imaging method provides pronounced enhancements in material contrast compared to single-modality imaging with conventional image processing (shown in top triangle with purple color scale).

subtracting an operational image with a dry reference image (*14*, *15*). With this work, we intend to extend the capabilities and spur innovation in high-contrast multimaterial and correlative characterization in static, dynamic, and operando applications. Furthermore, the detailed description of methods presented here is intended for transferable application to diverse fields, including but not limited to material science, earth science, porous media, and electrochemical energy devices, such as batteries and electrolyzers.

MATERIALS AND METHODS

Fuel cell hardware and setup

We use a custom fuel cell designed for simultaneous neutron and x-ray imaging (*55*). The fuel cell has an active area of 0.36 cm^2 and serpentine flow fields (6061 aluminum coated with 1.27 μm each of nickel and gold) with 0.5-mm-wide lands and channels and 0.4-mm-deep channels. The flow fields provide structural support to the MEA while maintaining pathways for the transport of fluids (through flow channels), electrons, and heat (through solid material). The MEA contains a commercial catalyst-coated Nafion 117 membrane (Ion Power, USA) with symmetric platinum loading of 0.3 mg cm^{-2} and commercial GDLs, SGL 25 BC (Sigracet GmbH, Germany) at the anode and cathode. The 177.8-μm-thick membrane is chosen to facilitate a detailed investigation of membrane hydration and morphological characteristics in operando fuel cells. The compression of GDLs is maintained using 152-μm-thick polytetrafluoroethylene sheets. Hydrogen and air are flowed at the anode and cathode, respectively, at an inlet relative humidity of 100%, flow rates of 0.2 liters/min, and back pressure of 100 kPa. High flow rates are used to prevent water slugs within the cathode channels. For this study, we focus our analysis on one testing condition to establish a robust methodology for material characterization: constant current density condition at 0.6 A cm^{-2} (measured cell temperature of 29°C) with humidified hydrogen and air flowing at the anode and cathode.

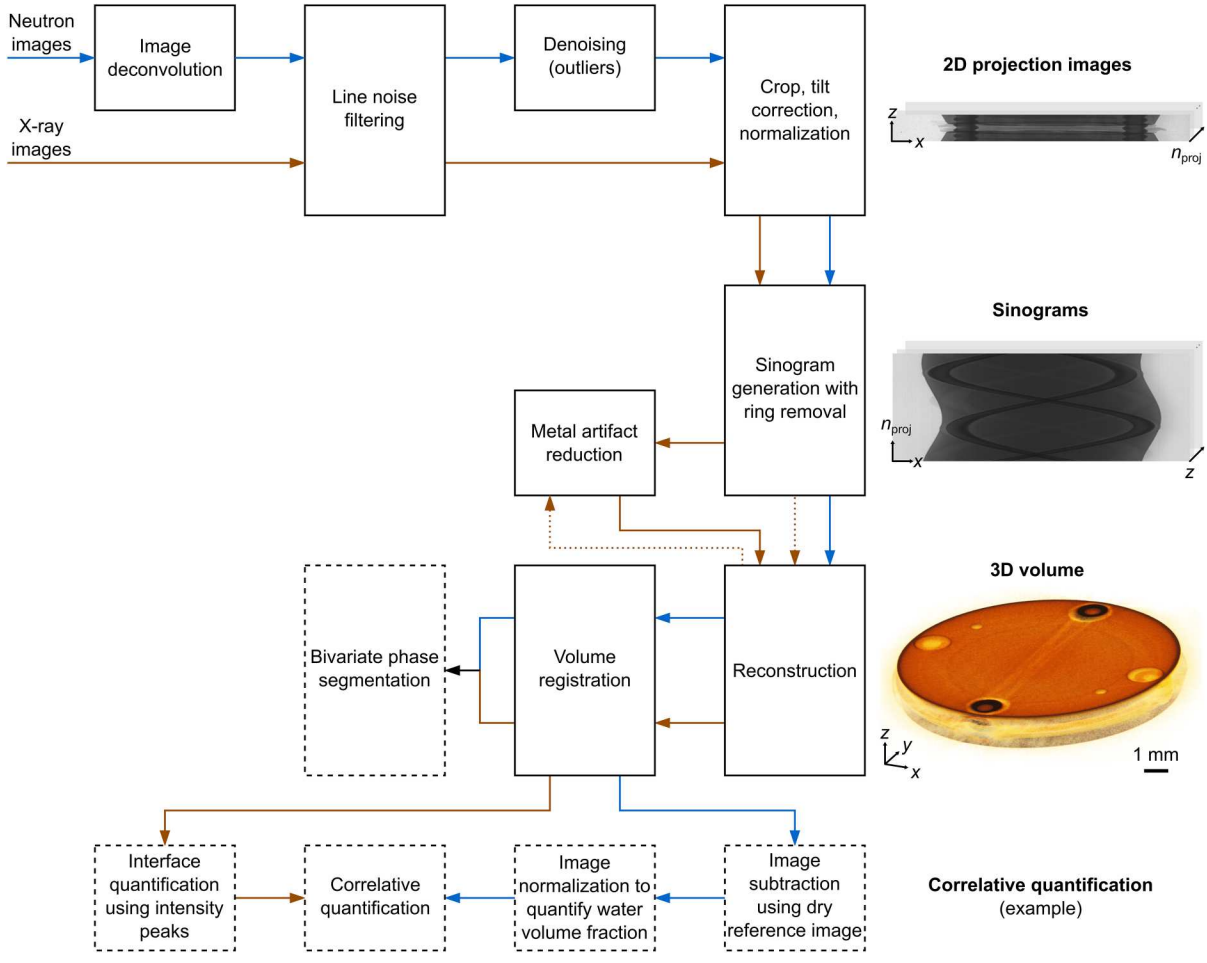

Fig. 7. Image processing sequence used on neutron (blue lines) and x-ray (brown lines) images. 2D projection images are obtained as an average of three projection images (with a spatial median filter of 3 pixels by 3 pixels). 2D projection images are converted into sinograms, which are then reconstructed into 3D volumes. Sample x-ray projection image, sinogram, and 3D reconstruction are shown with respect to spatial axes (*x*, *y*, and *z*) and the number of projections (n_{proj}). The image processing steps detailed in this study are shown with solid boxes, while additional steps used for phase segmentation and correlative quantification are shown in dashed boxes. Settings used for each image processing step are detailed in Table 1.

Operando NeXT setup

Operando NeXT is conducted at the BT-2 beamline at the National Institute of Standards and Technology (NIST) Center for Neutron Research (schematically shown in Fig. 1A). Neutrons are obtained from the NIST facility, and x-rays are obtained from Oxford Instruments UltraBright 90-keV microfocus x-ray tube (*26*). The x-ray was set to 70 keV at 40 W. For both neutron and x-ray imaging, lens-coupled cameras are used with a GadOx [gadolinium oxysulfide doped with terbium (Gd_2O_2S:Tb)] scintillators. Andor Neo scientific complementary metal oxide semiconductor cameras are paired with each detector. To prevent interference between the neutron and x-ray signals, lead and Li-doped poly shielding are used for the neutron and x-ray detectors, respectively, and the x-ray beam is masked using a tungsten shield. Stainless steel bolts used in this study are hollowed out in the center by drilling through holes to reduce attenuation of x-ray beam by the bolts. The sizes of each voxel achieved using the setup are 8.94 and 8.45 μm for neutron and x-ray imaging, respectively. The fuel cell is rotated 360° during operation to collect 701 equally spaced 2D averaged projection images for both neutron and x-ray imaging. Each averaged projection image is obtained by averaging three projection images at an exposure time of 5 s (total scan time of around 4 hours). For this study, we focus on steady-state operando properties of component morphology and liquid water distribution. To ensure steady-state operation at a chosen current density, imaging is conducted during constant current steps after 15 min of stabilization. Transient evolution of liquid water distributions and fuel cell performance have been shown to stabilize within the chosen 15 min in similar testing conditions (*56*) and are not the focus of our current study. We use high-fidelity scanning with discrete tomographic projection steps rather than imaging during continuous rotation; the former technique is suited for steady-state processes, while the latter is better suited for dynamic processes. Image processing is used to further enhance contrast between materials (image processing routine is highlighted in Fig. 7 and detailed in the sections following). For this study, the acronym NeXT is used to refer to the tomographic technique of combining neutrons and x-rays. The work described in this study uses the NeXT-NIST setup at the NIST facility (Gaithersburg, USA) (*26*). Although the experiments here are conducted at the NIST beamline, other beamlines also have capabilities of combining neutrons and x-rays for tomography. At the time of publication, NeXT setups are also available at the Institut Laue-Langevin (Grenoble, France) (*27*) and the Imaging with Cold Neutrons facility in Paul Scherrer Institut (Villigen, Switzerland) (*28*). We anticipate the benefits of combining NeXT with advanced image processing to be transferrable to other beamlines and image processing methods.

Noise reduction in 2D projection images and Sinogram generation

To prepare 2D projection images for reconstruction and quantitative analysis, the projection images are denoised using custom graphical user interface–supported code from NIST (*26*, *57*) and Fiji (*58*). Each projection image is an average of three images with a spatial median filter of 3 pixels by 3 pixels. For neutron images, image deconvolution is applied to deblur projection images (*26*). Image deconvolution is used to correct for blurring caused by the detector point spread function, which represents nonideal spreading of a point source beam in neutron images (*59*). Both neutron and x-ray images are processed using a line filter (wavelet ring filter) to suppress ring artifacts in reconstructed volumes. An additional denoising step is applied to neutron images to remove artifacts with unrealistically high gray values. The projection images are then rotated to align the axis of rotation with the vertical axis, log-normalized by the intensity of background, and cropped to the region of interest. Dark-field and flat-field corrections are performed to account for camera noise and the nonuniform spatial distribution of incoming beam, respectively. The prepared projection images are converted to sinograms. Sinograms contain normalized projection data that is rearranged such that a 2D sinogram for each detector row position (z position in Fig. 7) contains detector column positions (x position in Fig. 7) on the horizontal axis and projection angles on the vertical axis (sample x-ray sinogram is shown in Fig. 7). Details of image settings are found in Table 1, while the procedure is schematically shown in Fig. 7. For additional details, readers are referred to a paper by LaManna *et al.* (*26*).

3D reconstruction

The sinograms are reconstructed into 3D volumes using two methods: (i) conventional FBP using Octopus (*60*) and (ii) SIRT using open-source ASTRA toolbox (*35*, *61*). FBP is an analytical reconstruction technique, in which the projection signals from all angular steps are back-projected onto the 3D volume. The signal is filtered in the Fourier space to enhance high frequencies and thereby deblur and sharpen the edges in 3D space. Mathematical details of FBP, including Fourier slice theorem, may be found in textbook by Banhart (*62*). FBP is a fast and convenient reconstruction technique but relies on a high number of projection angles and high-quality 2D projections for accurate reconstruction. In many practical applications, such as operando scans, when the number of projection angles or the quality of individual 2D projections is low, FBP is susceptible to noise and yields low-quality reconstructions.

Iterative reconstruction techniques are more noise-tolerant and robust when dealing with a limited number of projections or noisy projection images (*34*, *35*) and are better suited for operando imaging. For this study, we use an algebraic iterative reconstruction algorithm known as the SIRT (*35*, *40*). A key advantage of SIRT over FBP is that a feedback loop is used to iteratively correct the calculated reconstructed 3D volume by comparing actual measurements of 2D projections to calculated projections. In general, the algebraic problem of 3D reconstruction requires us to solve for an unknown 3D reconstructed volume, $\boldsymbol{v}$, using a series of measured 2D projections, $\boldsymbol{p}$, with a set of equations $W\boldsymbol{v} = \boldsymbol{p}$, where W is a projection matrix that captures how 3D volume geometry maps onto the 2D projection geometry (*35*). In SIRT, an initial reconstruction is assumed, typically as a 3D volume with a uniform voxel value of zero. At each iteration, the 3D reconstructed volume is virtually projected on the projection space (called forward projection) to obtain reprojections with the same angular spacing as the original measured 2D projections. The difference between the reprojections and measured projections is back-projected into 3D space and used to update the reconstructed volume for the next iteration. With each iteration, the SIRT algorithm attempts to reduce the deviation between the measured projection images and the calculated reprojected images to enable a more accurate mapping of measured 2D projections onto the calculated 3D space. This feedback mechanism helps reduce noise in the reconstructed volume with each

iteration, capturing a key advantage of SIRT over noniterative methods such as FBP. Mathematically, the algorithm updates the reconstructed volume at each iteration, $\boldsymbol{v_{k+1}}$ using the volume at the previous iteration, $\boldsymbol{v_k}$, the measured 2D projections, $\boldsymbol{p}$, and the projection matrix, W, using the equation

$$\boldsymbol{v_{k+1}} = \boldsymbol{v_k} + CW^T R(\boldsymbol{p} - W\boldsymbol{v_k}) \quad (1)$$

where C and R are diagonal matrices containing inverse column and row sums of W, respectively (*35*). For more details on SIRT and the mathematics of reconstruction, readers are referred to the work by van Aarle *et al.* (*35*, *61*) and Banhart (*62*). Following reconstruction, the positive gray values in each 3D image are normalized to a range between 0 and 1 to facilitate comparative analysis. Comparison of results of the two reconstruction techniques is presented in Results.

To visualize and render 3D volumes (Figs. 1, 5, and 6) and movies (movie S1), we use Dragonfly software (Object Research Systems, Montreal, Canada) (*63*), while 2D slices are visualized using Fiji (*58*).

Streak artifact reduction to preserve highly attenuating materials

Streak artifacts from stainless steel bolts are corrected for using a simple technique called MAR-LI. Although MAR-LI is particularly useful to correct for artifacts from highly attenuating metals in x-ray images, the technique may be extended to streaks from other highly attenuating materials (including nonmetals) in x-ray or neutron images (here, we only observed streaks from stainless steel bolts in x-ray images). The sinograms are first reconstructed using SIRT and thresholded to segment the metal bolts in 3D. This segmented metal image is then forward projected to create a sinogram of only the metal, called a metal trace. The metal trace is subtracted from the original sinogram, and gaps in the sinogram are filled using linear interpolation. This corrected sinogram is then reconstructed to obtain a 3D reconstruction without the presence of the metal and correspondingly with lower streak artifacts. Last, the metal bolts are added back to the 3D image using the segmented metal mask with the initial reconstruction to incorporate the metal bolts without streak artifacts from reconstruction. For this study, we use an open-source implementation of MAR-LI in MATLAB (*37*). In this study, advanced image processing refers to the image processing with SIRT and MAR-LI, while conventional image processing refers to the use of FBP during image processing. In this study, MAR-LI is applied with all SIRT reconstructions in our region of interest (MEA region), except for Fig. 4A (where MAR-LI is not applied on the SIRT reconstruction to highlight the benefits of MAR-LI).

Volume registration of neutron and x-ray images in 3D

To correlate information obtained from neutron and x-ray imaging, 3D multimodal volume registration is conducted, whereby the x-ray images are scaled and transformed to align with the neutron images. A preliminary registration is conducted manually in Fiji (*58*) to coarsely align the two volumes. Fine volume registration, including translation, rotation, and scaling in 3D, is conducted using a custom MATLAB code from NIST (*26*). The transformation matrix required for fine registration is found using 3D volumes that are downsampled by a factor of 5^3 (each dimension by a factor of 5) to save memory and enhance registration quality through blurring. The transformation matrix is applied to the pre-downsampled x-ray images to obtained registered volumes. Similar implementations of multimodal registration and analysis may be accomplished using open-source software, e.g., (*64*).

Quantitative analysis of signal and contrast

The quality of 3D volumes is quantitatively assessed using SNR and CNR. SNR and CNR are calculated for specific materials of interest, e.g., liquid water droplets or CL. We identify a region within the 3D image that contains the material of interest exclusively and use the region to calculate mean and SD in gray values (GV) for the material, labeled mean_{GV} and sd_{GV}, respectively. CNR and SNR are calculated as

$$\text{SNR} = \frac{\text{mean}_{\text{GV}}}{\text{sd}_{\text{GV}}} \quad (2)$$

$$\text{CNR}_{\text{AB}} = \frac{\text{mean}_{\text{GV,A}} - \text{mean}_{\text{GV,B}}}{\sqrt{[(\text{sd}_{\text{GV,A}})^2 + (\text{sd}_{\text{GV,B}})^2]/2}} \quad (3)$$

where subscripts A and B are used to denote two materials of interest for which the CNR is calculated. High SNR is an indication of high quality of signal gray value with respect to noise. High CNR between materials indicates high contrast and discernability between materials in 3D volume and is desirable for quantitative analysis.

To assess the benefits of combining dual-modality imaging and advanced image processing, a correlative contrast matrix is generated (Figs. 5B and 6B and fig. S3). CNR between each pair of components (of interest) is calculated for each modality and the imaging modality (x-ray or neutron) with higher CNR is chosen as the "dominant" modality to distinguish between the given material pair; the other imaging modality is labeled "unused" modality for the given material pair. In the contrast matrix, the bottom left region (in green) shows the CNR for the dominant imaging modality. When the dominant imaging modality is neutron imaging, the CNR is indicated with a * symbol. The benefit of advanced image processing over conventional image processing is quantified by comparing CNRs calculated using advanced and conventional image processing for the dominant image modality (top right triangle in fig. S3). To highlight and quantify the compounding benefits of combining dual-modality imaging with advanced processing, CNRs of the dominant modality with advanced image processing are compared to CNRs of the unused modality with conventional FBP processing (top right triangle in Figs. 5B and 6B).

Supplementary Materials

This PDF file includes:

Figs. S1 to S3
Tables S1 and S2
Legend for movie S1

Other Supplementary Material for this manuscript includes the following:

Movie S1

REFERENCES AND NOTES

1. P. J. Withers, C. Bouman, S. Carmignato, V. Cnudde, D. Grimaldi, C. K. Hagen, E. Maire, M. Manley, A. Du Plessis, S. R. Stock, X-ray computed tomography. *Nat Rev Methods Primers* **1**, 18 (2021).
2. X. Liu, A. Ronne, L.-C. Yu, Y. Liu, M. Ge, C.-H. Lin, B. Layne, P. Halstenberg, D. S. Maltsev, A. S. Ivanov, S. Antonelli, S. Dai, W.-K. Lee, S. M. Mahurin, A. I. Frenkel, J. F. Wishart, X. Xiao, Y. K. Chen-Wiegart, Formation of three-dimensional bicontinuous structures via molten salt dealloying studied in real-time by in situ synchrotron X-ray nano-tomography. *Nat. Commun.* **12**, 3441 (2021).
3. R. F. Ziesche, T. Arlt, D. P. Finegan, T. M. M. Heenan, A. Tengattini, D. Baum, N. Kardjilov, H. Markötter, I. Manke, W. Kockelmann, D. J. L. Brett, P. R. Shearing, 4D imaging of lithium-batteries using correlative neutron and X-ray tomography with a virtual unrolling technique. *Nat. Commun.* **11**, 777 (2020).
4. A. Ulvestad, A. Singer, J. N. Clark, H. M. Cho, J. W. Kim, R. Harder, J. Maser, Y. S. Meng, O. G. Shpyrko, Topological defect dynamics in operando battery nanoparticles. *Science* **348**, 1344–1347 (2015).
5. X. Peng, D. Kulkarni, Y. Huang, T. J. Omasta, B. Ng, Y. Zheng, L. Wang, J. M. LaManna, D. S. Hussey, J. R. Varcoe, I. V. Zenyuk, W. E. Mustain, Using operando techniques to understand and design high performance and stable alkaline membrane fuel cells. *Nat. Commun.* **11**, 3561 (2020).
6. D. R. Baker, F. Brun, C. O'Shaughnessy, L. Mancini, J. L. Fife, M. Rivers, A four-dimensional X-ray tomographic microscopy study of bubble growth in basaltic foam. *Nat. Commun.* **3**, 1135 (2012).
7. Y. Haridy, M. Osenberg, A. Hilger, I. Manke, D. Davesne, F. Witzmann, Bone metabolism and evolutionary origin of osteocytes: Novel application of FIB-SEM tomography. *Sci. Adv.* **7**, eabb9113 (2021).
8. K. L. White, J. Singla, V. Loconte, J.-H. Chen, A. Ekman, L. Sun, X. Zhang, J. P. Francis, A. Li, W. Lin, K. Tseng, G. McDermott, F. Alber, A. Sali, C. Larabell, R. C. Stevens, Visualizing subcellular rearrangements in intact β cells using soft x-ray tomography. *Sci. Adv.* **6**, eabc8262 (2020).
9. L. Vásárhelyi, Z. Kónya, Á. Kukovecz, R. Vajtai, Microcomputed tomography–based characterization of advanced materials: A review. *Mat. Today Adv.* **8**, 100084 (2020).
10. J. Miao, P. Ercius, S. J. L. Billinge, Atomic electron tomography: 3D structures without crystals. *Science* **353**, aaf2157 (2016).
11. T. Cocquyt, Z. Zhou, J. Plomp, L. van Eijck, Neutron tomography of Van Leeuwenhoek's microscopes. *Sci. Adv.* **7**, eabf2402 (2021).
12. M. Jacot-Guillarmod, K. Schmidt-Ott, D. Mannes, A. Kaestner, E. Lehmann, C. Gervais, Multimodal tomography to assess dechlorination treatments of iron-based archaeological artifacts. *Herit. Sci.* **7**, 29 (2019).
13. J. Martell, C. Alwmark, L. Daly, S. Hall, S. Alwmark, R. Woracek, J. Hektor, L. Helfen, A. Tengattini, M. Lee, The scale of a martian hydrothermal system explored using combined neutron and x-ray tomography. *Sci. Adv.* **8**, eabn3044 (2022).
14. P. Shrestha, C. Lee, K. F. Fahy, M. Balakrishnan, N. Ge, A. Bazylak, Formation of liquid water pathways in PEM fuel cells: A 3-D pore-scale perspective. *J. Electrochem. Soc.* **167**, 054516 (2020).
15. H. Xu, S. Nagashima, H. P. Nguyen, K. Kishita, F. Marone, F. N. Büchi, J. Eller, Temperature dependent water transport mechanism in gas diffusion layers revealed by subsecond *operando* X-ray tomographic microscopy. *J. Power Sources* **490**, 229492 (2021).
16. S. S. Alrwashdeh, I. Manke, H. Markötter, M. Klages, M. Göbel, J. Haußmann, J. Scholta, J. Banhart, In operando quantification of three-dimensional water distribution in nanoporous carbon-based layers in polymer electrolyte membrane fuel cells. *ACS Nano* **11**, 5944–5949 (2017).
17. R. F. Ziesche, J. Hack, L. Rasha, M. Maier, C. Tan, T. M. M. Heenan, H. Markötter, N. Kardjilov, I. Manke, W. Kockelmann, D. J. L. Brett, P. R. Shearing, High-speed 4D neutron computed tomography for quantifying water dynamics in polymer electrolyte fuel cells. *Nat. Commun.* **13**, 1616 (2022).
18. Q. Meyer, Y. Zeng, C. Zhao, In situ and operando characterization of proton exchange membrane fuel cells. *Adv. Mater* **31**, 1901900 (2019).
19. Improving the fundamental understanding of batteries via *operando* measurements. *Nat. Commun.* **13**, 4723 (2022).
20. A. Kaestner, M. Morgano, J. Hovind, E. Lehmann, Bimodal imaging using neutrons and x-rays, paper presented at the Proceedings of the International Symposium on Digital Industrial Radiology and Computed Tomography, Belgium, Ghent, 22 to 25 June 2015; www.ndt.net/events/DIR2015/Paper/58_Kaestner.pdf.
21. H. J. Prask, J. M. Rowe, J. J. Rush, I. G. Schröder, The NIST cold neutron research facility. *J. Res. Inst. Stand. Technol.* **98**, 1–13 (1993).
22. M. Siegwart, R. Woracek, J. I. Márquez Damián, A. S. Tremsin, V. Manzi-Orezzoli, M. Strobl, T. J. Schmidt, P. Boillat, Distinction between super-cooled water and ice with high duty cycle time-of-flight neutron imaging. *Rev. Sci. Instrum.* **90**, 103705 (2019).
23. K. Jiao, J. Xuan, Q. Du, Z. Bao, B. Xie, B. Wang, Y. Zhao, L. Fan, H. Wang, Z. Hou, S. Huo, N. P. Brandon, Y. Yin, M. D. Guiver, Designing the next generation of proton-exchange membrane fuel cells. *Nature* **595**, 361–369 (2021).
24. D. A. Cullen, K. C. Neyerlin, R. K. Ahluwalia, R. Mukundan, K. L. More, R. L. Borup, A. Z. Weber, D. J. Myers, A. Kusoglu, New roads and challenges for fuel cells in heavy-duty transportation. *Nat. Energy* **6**, 462–474 (2021).
25. C. Tötzke, N. Kardjilov, N. Lenoir, I. Manke, S. E. Oswald, A. Tengattini, What comes NeXT? – High-speed neutron tomography at ILL. *Opt. Express* **27**, 28640–28648 (2019).
26. J. M. LaManna, D. S. Hussey, V. H. DiStefano, E. Baltic, D. L. Jacobson, "NIST NeXT: A system for truly simultaneous neutron and X-ray tomography" in *Hard X-Ray, Gamma-Ray, and Neutron Detector Physics XXII* (International Society for Optics and Photonics, 2020), vol. 11494, p. 114940P.
27. A. Tengattini, N. Lenoir, E. Andò, B. Giroud, D. Atkins, J. Beaucour, G. Viggiani, NeXT-Grenoble, the Neutron and X-ray tomograph in Grenoble. *Nucl. Instrum. Methods Phys. Res., Sect. A* **968**, 163939 (2020).
28. A. P. Kaestner, J. Hovind, P. Boillat, C. Muehlebach, C. Carminati, M. Zarebanadkouki, E. H. Lehmann, Bimodal imaging at ICON using neutrons and X-rays. *Physics Procedia* **88**, 314–321 (2017).
29. E. Stavropoulou, E. Andò, A. Tengattini, M. Briffaut, F. Dufour, D. Atkins, G. Armand, Liquid water uptake in unconfined Callovo Oxfordian clay-rock studied with neutron and X-ray imaging. *Acta Geotech.* **14**, 19–33 (2019).
30. M. Yusuf, J. LaManna, P. P. Paul, D. N. Agyeman-Budu, C. Cao, A. R. Dunlop, A. N. Jansen, B. J. Polzin, S. E. Trask, T. R. Tanim, E. J. Dufek, V. Thampy, H.-G. Steinrück, M. F. Toney, J. N. Weker, Simultaneous neutron and X-ray tomography for ex-situ 3D visualization of graphite anode degradation in extremely fast-charged lithium-ion batteries. *SSRN Electron. J.*, (2022).
31. E. Roubin, E. Andò, S. Roux, The colours of concrete as seen by X-rays and neutrons. *Cem. Concr. Compos.* **104**, 103336 (2019).
32. L. E. Dalton, J. M. LaManna, S. Jones, M. Pour-Ghaz, Does ITZ influence moisture transport in concrete? *Transp Porous Med.* **144**, 623–639 (2022).
33. H. Xu, M. Bührer, F. Marone, T. J. Schmidt, F. N. Büchi, J. Eller, Optimal image denoising for in situ X-ray tomographic microscopy of liquid water in gas diffusion layers of polymer electrolyte fuel cells. *J. Electrochem. Soc.* **167**, 104505 (2020).
34. W. Stiller, Basics of iterative reconstruction methods in computed tomography: A vendor-independent overview. *Eur. J. Radiol.* **109**, 147–154 (2018).
35. W. van Aarle, W. J. Palenstijn, J. Cant, E. Janssens, F. Bleichrodt, A. Dabravolski, J. D. Beenhouwer, K. J. Batenburg, J. Sijbers, Fast and flexible X-ray tomography using the ASTRA toolbox. *Opt. Express* **24**, 25129–25147 (2016).
36. D. Kazantsev, F. Bleichrodt, T. van Leeuwen, A. Kaestner, P. J. Withers, K. J. Batenburg, P. D. Lee, A novel tomographic reconstruction method based on the robust Student's t function for suppressing data outliers. *IEEE Trans. Comput. Imaging* **3**, 682–693 (2017).
37. Y. Zhang, H. Yu, Convolutional neural network based metal artifact reduction in x-ray computed tomography. *IEEE Trans. Med. Imaging* **37**, 1370–1381 (2018).
38. M. Katsura, J. Sato, M. Akahane, A. Kunimatsu, O. Abe, Current and novel techniques for metal artifact reduction at CT: Practical guide for radiologists. *Radiographics* **38**, 450–461 (2018).
39. B. Münch, P. Trtik, F. Marone, M. Stampanoni, Stripe and ring artifact removal with combined wavelet — Fourier filtering. *Opt. Express* **17**, 8567–8591 (2009).
40. M. Bührer, H. Xu, J. Eller, J. Sijbers, M. Stampanoni, F. Marone, Unveiling water dynamics in fuel cells from time-resolved tomographic microscopy data. *Sci. Rep.* **10**, 16388 (2020).
41. J. Tuszynski, Photon Attenuation. MATLAB Central File Exchange; www.mathworks.com/matlabcentral/fileexchange/12092-photonattenuation.
42. X-Ray Mass Attenuation Coefficients. NIST (2009); www.nist.gov/pml/x-ray-mass-attenuation-coefficients.
43. XCOM: Photon Cross Sections Database. NIST (2009); www.nist.gov/pml/xcom-photon-cross-sections-database.
44. Neutron scattering lengths and cross sections, www.ncnr.nist.gov/resources/n-lengths/.
45. V. F. Sears, Neutron scattering lengths and cross sections. *Neutron News* **3**, 26–37 (1992).
46. H. Markötter, I. Manke, J. Böll, S. Alrwashdeh, A. Hilger, M. Klages, J. Haussmann, J. Scholta, Morphology correction technique for tomographic in-situ and operando studies in energy research. *J. Power Sources* **414**, 8–12 (2019).
47. B. De Man, J. Nuyts, P. Dupont, G. Marchal, P. Suetens, Metal streak artifacts in X-ray computed tomography: A simulation study. *IEEE Trans. Nucl. Sci.* **46**, 691–696 (1999).
48. B. Zhou, X. Chen, S. K. Zhou, J. S. Duncan, C. Liu, DuDoDR-Net: Dual-domain data consistent recurrent network for simultaneous sparse view and metal artifact reduction in computed tomography. *Med. Image Anal.* **75**, 102289 (2022).
49. Y. Singh, R. T. White, M. Najm, T. Haddow, V. Pan, F. P. Orfino, M. Dutta, E. Kjeang, Tracking the evolution of mechanical degradation in fuel cell membranes using 4D in situ visualization. *J. Power Sources* **412**, 224–237 (2019).

50. P. Boillat, D. Kramer, B. C. Seyfang, G. Frei, E. Lehmann, G. G. Scherer, A. Wokaun, Y. Ichikawa, Y. Tasaki, K. Shinohara, In situ observation of the water distribution across a PEFC using high resolution neutron radiography. *Electrochem. Commun.* **10**, 546–550 (2008).
51. A. Tengattini, N. Kardjilov, L. Helfen, P.-A. Douissard, N. Lenoir, H. Markötter, A. Hilger, T. Arlt, M. Paulisch, T. Turek, I. Manke, Compact and versatile neutron imaging detector with sub-4μm spatial resolution based on a single-crystal thin-film scintillator. *Opt. Express* **30**, 14461–14477 (2022).
52. Y.-C. Chen, A. Berger, S. De Angelis, T. Schuler, M. Bozzetti, J. Eller, V. Tileli, T. J. Schmidt, F. N. Büchi, A method for spatial quantification of water in microporous layers of polymer electrolyte fuel cells by X-ray tomographic microscopy. *ACS Appl. Mater. Interfaces* **13**, 16227–16237 (2021).
53. T. Bultreys, M. A. Boone, M. N. Boone, T. De Schryver, B. Masschaele, L. Van Hoorebeke, V. Cnudde, Fast laboratory-based micro-computed tomography for pore-scale research: Illustrative experiments and perspectives on the future. *Adv. Water Resour.* **95**, 341–351 (2016).
54. Y. D. Wang, Q. Meyer, K. Tang, J. E. McClure, R. T. White, S. T. Kelly, M. M. Crawford, F. Iacoviello, D. J. L. Brett, P. R. Shearing, P. Mostaghimi, C. Zhao, R. T. Armstrong, Large-scale physically accurate modelling of real proton exchange membrane fuel cell with deep learning. *Nat. Commun.* **14**, 745 (2023).
55. J. LaManna, Three-dimensional water distribution and interfacial effects through simultaneous neutron and x-ray tomography, paper presented at 232nd ECS Meeting, National Harbor, MD, 1 to 5 October 2017; https://ecs.confex.com/ecs/232/webprogram/Paper105418.html.
56. R. Banerjee, N. Ge, J. Lee, M. G. George, S. Chevalier, H. Liu, P. Shrestha, D. Muirhead, A. Bazylak, Transient liquid water distributions in polymer electrolyte membrane fuel cell gas diffusion layers observed through in-operando synchrotron x-ray radiography. *J. Electrochem. Soc.* **164**, F154–F162 (2017).
57. J. M. LaManna, D. S. Hussey, E. Baltic, D. L. Jacobson, Neutron and X-ray tomography (NeXT) system for simultaneous, dual modality tomography. *Rev. Sci. Instrum.* **88**, 113702 (2017).
58. J. Schindelin, I. Arganda-Carreras, E. Frise, V. Kaynig, M. Longair, T. Pietzsch, S. Preibisch, C. Rueden, S. Saalfeld, B. Schmid, J.-Y. Tinevez, D. J. White, V. Hartenstein, K. Eliceiri, P. Tomancak, A. Cardona, Fiji: An open-source platform for biological-image analysis. *Nat. Methods* **9**, 676–682 (2012).
59. D. S. Hussey, D. Spernjak, A. Z. Weber, R. Mukundan, J. Fairweather, E. L. Brosha, J. Davey, J. S. Spendelow, D. L. Jacobson, R. L. Borup, Accurate measurement of the through-plane water content of proton-exchange membranes using neutron radiography. *J. Appl. Phys.* **112**, 104906 (2012).
60. M. Dierick, B. Masschaele, L. V. Hoorebeke, Octopus, a fast and user-friendly tomographic reconstruction package developed in LabView. *Meas. Sci. Technol.* **15**, 1366–1370 (2004).
61. W. van Aarle, W. J. Palenstijn, J. De Beenhouwer, T. Altantzis, S. Bals, K. J. Batenburg, J. Sijbers, The ASTRA Toolbox: A platform for advanced algorithm development in electron tomography. *Ultramicroscopy* **157**, 35–47 (2015).
62. J. Banhart, *Monographs on the Physics and Chemistry of Materials Advanced Tomographic Methods in Materials Research and Engineering* (Oxford University Press, 2008).
63. Dragonfly (2020). [Computer]. Object Research Systems (ORS) Inc., Montreal, Canada, 2020; www.theobjects.com/dragonfly.
64. O. Stamati, E. Andò, E. Roubin, R. Cailletaud, M. Wiebicke, G. Pinzon, C. Couture, R. C. Hurley, R. Caulk, D. Caillerie, T. Matsushima, P. Besuelle, F. Bertoni, T. Arnaud, A. O. Laborin, R. Rorato, Y. Sun, A. Tengattini, O. Okubadejo, J.-B. Colliat, M. Saadatfar, F. E. Garcia, C. Papazoglou, I. Vego, S. Brisard, J. Dijkstra, G. Birmpilis, Spam: Software for practical analysis of materials. *J. Open Source Softw.* **5**, 2286 (2020).
65. V. Patel, R. N. Chityala, K. R. Hoffmann, C. N. Ionita, D. R. Bednarek, S. Rudin, Self-calibration of a cone-beam micro-CT system. *Med. Phys.* **36**, 48–58 (2009).

Acknowledgments

Funding: Financial support from the Natural Sciences and Engineering Research Council of Canada (NSERC; Discovery Grant; to A.B.), the Canada Research Chairs Program (Canada Research Chair in Clean Energy; to A.B.), and the Canada Foundation for Innovation (Leaders Opportunity Fund; to A.B.) are gratefully acknowledged. Graduate scholarships from the Vanier Canada Graduate Scholarship (to P.S.), the Hatch Graduate Scholarship for Sustainable Energy Research (to P.S. and P.K.), and the Lachlan Gilchrist Fellowship Fund (to P.S.) are gratefully acknowledged. Graduate scholarships to P.K. from the Queen Elizabeth II/DuPont Canada Scholarship in Science and Technology and Hatch Graduate Scholarship for Sustainable Energy Research are gratefully acknowledged. Graduate scholarship awarded to J.K.L. from NSERC Alexander Graham Bell Canada Graduate Scholarship – Doctoral program is greatly acknowledged. Research described in this study was conducted at the National Institute for Standards and Technology (NIST). Partial funding was provided by the NIST Physical Measurement Laboratory, Radiation Physics Division, and Center for Neutron Research (to J.M. L., D.L.J., D.S.H., and E.B.). **Author contributions:** Conceptualization: P.S., A.B., and J.M.L. Investigation and analysis: P.S. Design of NIST-NeXT system: J.M.L., D.L.J., D.S.H., and E.B. Experimentation and visualization: P.S., J.M.L., K.F.F., P.K., C.H.L., J.K.L., E.B., D.L.J., D.S.H., and A.B. Supervision: A.B. Writing—original draft: P.S. Writing—review and editing: P.S., J.M.L., K.F.F., P.K., C.H.L., J.K.L., E.B., D.L.J., D.S.H., and A.B. **Competing interests:** Certain trade names and company products are mentioned in the text or identified in an illustration to adequately specify the experimental procedure and equipment used. In no case does such identification imply recommendation or endorsement by the National Institute of Standards and Technology, nor does it imply that the products are necessarily the best available for the purpose. The authors declare that they have no other competing interests. **Data and materials availability:** All data needed to evaluate the conclusions in the paper are present in the paper and/or the Supplementary Materials.

Submitted 26 January 2023
Accepted 6 October 2023
Published 8 November 2023
10.1126/sciadv.adg8634